

The CLAS12 RICH Detector

Abstract

A Ring Imaging Cherenkov detector has been installed on the CLAS12 spectrometer at the Jefferson Laboratory (JLab) to provide the experiment with kaon identification in the momentum range between 3 and 8 GeV/c. The detector adopts a hybrid optics solution with aerogel radiator, light planar and spherical mirrors and highly-segmented photon detectors. We report here on the design, construction and initial performance of the RICH during the commissioning of the detector and the first physics data taking.

Keywords: Ring-imaging Cherenkov detectors, Single-photon detection, Front-end electronics, Multi-anode PMT, Aerogel radiator, Carbon-fiber and glass-skin mirrors

1. The CLAS12 Experiment

The Continuous Electron Beam Accelerator Facility (CEBAF) and associated experimental equipment at Jefferson Lab (JLab) comprise a unique facility for nuclear physics research whose upgrade was completed in 2017. The upgraded facility will accelerate high current and a high polarized electron beams to 11 GeV for experiments in the existing Halls A, B and C. In addition, a 12 GeV beam is provided to a new experimental hall, Hall D, to generate a 9 GeV tagged photon beam. The upgrade includes beam line and equipments in the existing halls.

In the Hall B, the new CLAS12 spectrometer [1] has been installed, which allows detection of charged and neutral particles in a wide kinematic range with maximum instantaneous luminosity of the order of $10^{35} \text{ cm}^{-2}\text{s}^{-1}$. The physics program of CLAS12 is broad and covers many aspects of the hadron physics: nucleon structure, baryon and meson spectroscopy and search for exotic states [2].

CLAS12 is a magnetic spectrometer based on a toroidal field produced by six superconducting coils that naturally divide the spectrometer in six independent sectors. Each sector is instrumented with several subdetectors. Three regions of Drift Chambers allow the measurement of the charged particle momentum, while threshold Cherenkov counters, time-of-flight (TOF) detectors and electromagnetic calorimeters are used for particle identification.

The first module of a Ring Imaging Cherenkov (RICH) detector, that was designed to allow the identification of kaons against protons and pions in the momentum range between 3 and 8 GeV/c, was completed before the start of the physics run, see Fig. 1. For the completion of the approved physics program [3], the installation of a second module in the opposite sector is foreseen for the beginning of the CLAS12 operation with polarized targets.

2. The CLAS12 Ring-Imaging Cherenkov Detector

In the CLAS12 kinematic regime, the expected production ratio of kaons to pions is about 1 to 10. Therefore, in order to

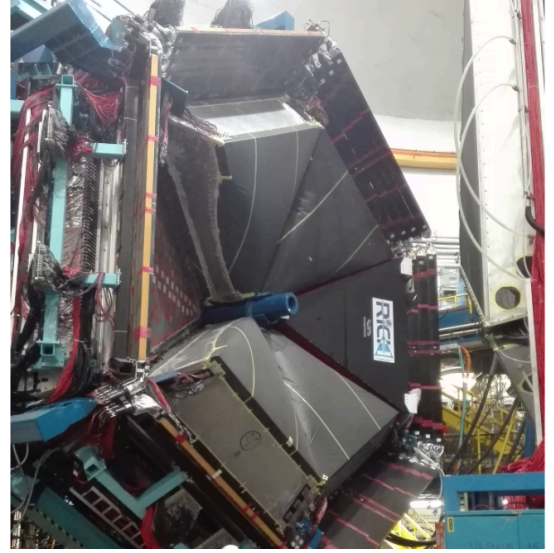


Figure 1: The first module of the CLAS12 RICH installed in sector 4 of the Hall-B forward carriage

keep the contamination of misidentified kaons at a few percent level, a pion to kaon rejection power of the order of 1:500 is required.

The design of a RICH detector with these performances within the CLAS12 constraints was challenging, because of the peculiar trapezoidal shape and the stringent requirements in terms of material budget imposed by the downstream TOF and calorimeters detectors. Therefore, an effort was made in order to reduce the inactive material as much as possible. In addition, its large size (about 5 m^2 entrance window) imposed to reduce the area instrumented with photodetectors in order to contain the costs at an affordable level.

Simulation studies [4, 5] and test of various prototypes with hadron beams [6] led to a non conventional proximity focusing geometry, incorporating an aerogel radiator, a system of planar and spherical mirrors and visible light photodetectors, in which

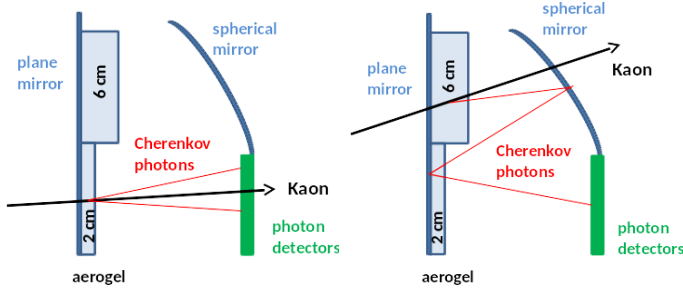


Figure 2: A schematic drawing of the CLAS12 RICH, whose hybrid optics design exploits direct imaging and light reflections to extend the angular and momentum coverage while limiting the active area to only about 1 squared meter.

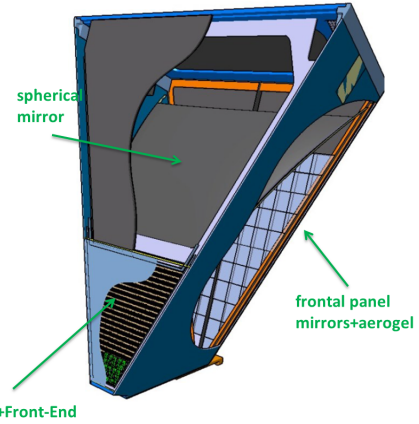


Figure 4: A schematic drawing of the CLAS12 RICH with the internal components highlighted.

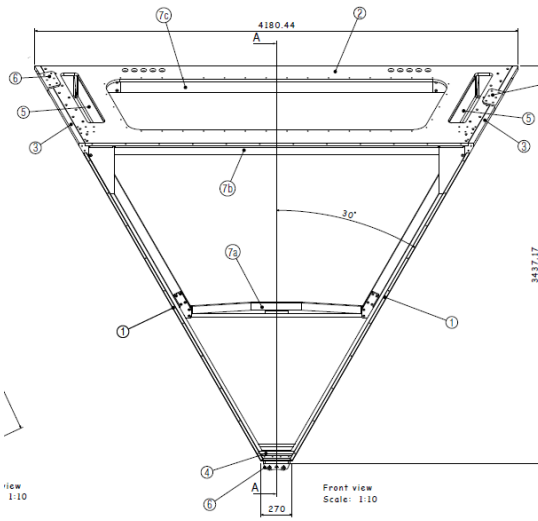


Figure 3: The composite frame of the RICH detector. The components inside the CLAS12 acceptance (2, 7a, 7b, 7c) are made by carbon fiber.

the Cherenkov photons can be detected either directly or after reflections on the mirrors. A sketch of the detector is shown in Fig. 2.

2.1. The Mechanical Structure

The mechanical structure of the RICH, produced by the *Tecnologie Avanzate* [7] company, utilizes aluminum for the elements in the dead volume of CLAS12 and carbon fiber for the elements inside of the CLAS12 acceptance, see Fig. 3. For all the parts with large dimensions, the sandwich technique was used, in which two thin solid skins are glued together on a honeycomb core. The RICH mechanical structure was assembled on a frame especially designed to allow the installation of the internal components and of the closing panels, see Fig. 4. Special attention was devoted to the structure rigidity to minimize stress and misalignments of the delicate optical components (mirrors and aerogel) during the assembly, transportation and installation.

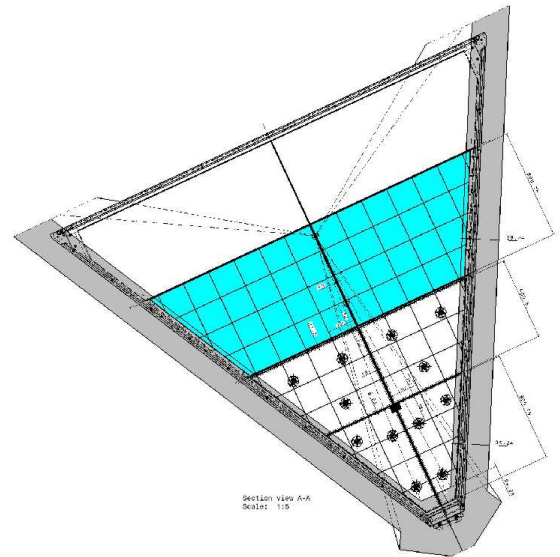


Figure 5: The aerogel tile configuration. The edge tiles have been shaped to match the RICH geometry. The 6 cm section (cyan) is made by two layers of 30 mm thick aerogel tiles installed on the front carbon fiber panel. One layer of 20 mm thick aerogel tiles is mounted on the two front mirrors in the region close to the beam pipe. The aerogel is secured in place by a grid of nylon wires stretched on a 2 mm Aluminum perimetral frame. The mirror mounting points has been designed to stay outside the CLAS12 acceptance.

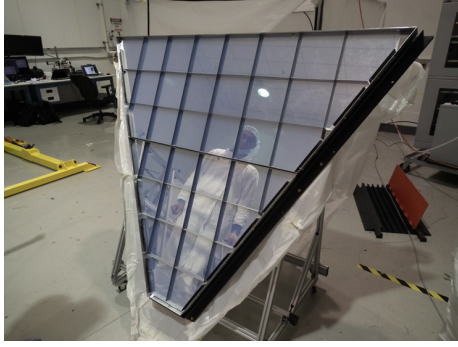


Figure 6: The 20 mm thickness section of the aerogel.

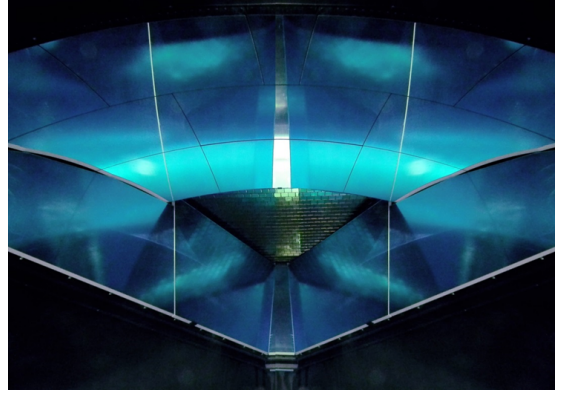


Figure 7: The mirror system as it is seen from the RICH entrance panel.

2.2. The Aerogel Radiator

In the few GeV/c momentum range, the best radiator option is silica aerogel, which is being used by several particle and nuclear physics experiments worldwide [8, 9]. The aerogel radiator used in the CLAS12 RICH is made by 102 large tiles with nominal refractive index $n = 1.05$ produced by the *Budker and Boreskov Institute of Nuclear Physics* (Russia). In order to match the RICH geometry, the tiles were cut with squared $200 \times 200 \text{ mm}^2$ as well as pentagonal, trapezoidal and triangular shape, see Fig. 5. The tiles are assembled in two separate sections. In the most forward section, the tiles have thickness of 20 mm and are installed on top of the frontal planar mirrors. In the large angle sections, two layers of 30 mm thickness tiles are installed on the carbon fiber entrance panel of the RICH. Fig. 6 shows the 20 mm sections of the aerogel wall fully assembled.

A series of characterization measurements [10] was performed in order to determine the main optical and geometrical parameters of all the tiles. The results showed that all the tiles satisfied the required specifications. In particular, using the Hunt parametrization of the light transmission [11], the average values obtained over all the tiles are scattering length of $L_{\text{scatt}} = 50.5 \text{ mm}$, transparency parameter $A_0 = 0.975$ and clarity parameter $C = 0.00512 \mu\text{m}^4/\text{cm}$. From these measurements, the expected photon yield for $\beta = 1$ particles was computed and the tiles with highest yield were installed where the more demanding rejection power is expected.

2.3. The Mirror System

The mirror system is composed by 10 spherical mirrors, installed just before the exit panel of the RICH, and 7 planar mirrors installed on the entrance and lateral panels. The system was designed to minimize the photon loss and to direct as much as possible of the Cherenkov radiation toward the photodetectors. The mirror system as it is seen from the entrance panel is shown in Fig. 7.

The spherical mirrors, produced by the *Composite Mirror Applications* company [12], are made by two layers of carbon fiber glued on a honeycomb core and were coated with the reflecting layer by the *Evaporated Coatings Inc* [13]. The total area of these mirrors is about 3.5 m^2 . The accuracy of the spherical surface was verified through the reflected spot size



Figure 8: The spherical mirror before (left) and after (right) alignment.

measurements, which also provides the average radius of curvature. All the mirrors exhibit a spot size smaller than 1.5 mm and a mirror-to-mirror variation in the radius below 0.5%, well within the required specifications.

The planar mirrors, produced by the *Media Lario* company [14], are made by two thin layers of glass glued on a aluminum honeycomb core. Being in the acceptance of the detector, the frontal mirrors use very thin (0.7 mm) glass layers, while for the lateral ones thicker (1.6 mm) layers were used. This technology, used for the first time in nuclear physics experiments, allows to have mirrors with material budget comparable to the carbon fiber ones, but at much lower cost. The total area of the mirrors is about 6.5 m^2 . The planarity of the mirror surface was measured by using a Coordinate Measuring Machine (CMM). Typically, the measured surface accuracy is of the order of few microns RMS, corresponding to a contribution to the angular resolution below 0.1 mrad, by far within the required specification of 0.3 mrad.

The characterization of both spherical and planar mirrors was completed by reflectivity measurements on several sample spots on the mirror surface in the range of wavelengths of interest from 350 to 600 nm. For all the mirrors, we obtained on average a reflectivity between 88% and 90%.

The planar mirror were aligned with respect the RICH structure with a precision of 0.1 mrad with the use of a CMM machine. The spherical mirrors were aligned with a precision bet-

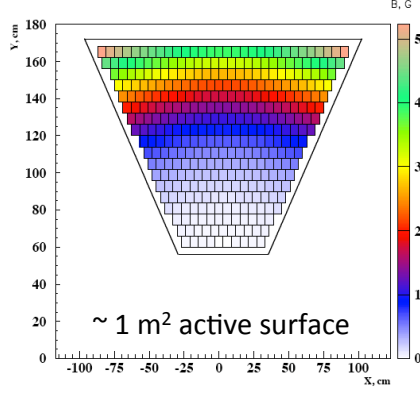


Figure 9: The RICH photon detector area with the simulated torus fringe field strength.

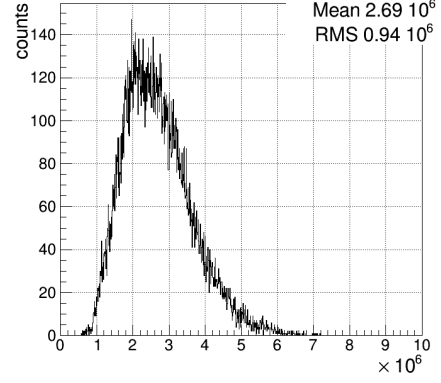


Figure 10: Distribution of the data-sheet gains of the 25000 RICH MAPMT channels.

ter than 0.1 mrad by converging the spot images of a pointlike source on the nominal center position, imaged by a XIMEA camera with a 1 cm wide CMOS sensor, see Fig. 8.

2.4. The Photon Detector

The goal of the CLAS12 RICH is to achieve a single photon-electron (SPE) Cherenkov angle resolution, dominated by the aerogel chromatic dispersion, of 4.5 mrad. At the RICH detector position, the CLAS12 torus fringe field is low enough to allow a flexible choice of the photosensor technology, see Fig. 9. The flat panel Hamamatsu H8500 Multi-Anode PhotoMultiplier Tube (MaPMT) [15] has been selected to achieve the design angular resolution, thanks to the enhanced sensitivity to the visible and near-UV light in conjunction with a matching geometrical layout of 64 pixels covering a $5 \times 5 \text{ cm}^2$ area with an excellent packing factor of 89%. Despite not advertised as the optimal choice in the SPE regime, such MaPMT showed adequate performance in several laboratory tests [16] and at beam tests [6] when used in conjunction with an adapted readout electronics. Just after the RICH construction startup, the novel Hamamatsu H12700 became available, with the same layout of the H8500 but an optimized dynode structure for single photon detection [17].

The CLAS12 RICH is the first large-area detector to employ this type of multi-anode photo-multiplier. A total of 391 MAPMTs, corresponding to about 25000 pixels, are needed to cover the about 1 m^2 trapezoidal active area of the first RICH module. The production of the RICH photon detectors (80 H8500 and 320 H12700) has been completed, achieving an average gain of $2.7 \cdot 10^6$, which corresponds to about 400 fC generated charge per SPE, see Fig. 10.

2.5. The Readout Electronics

The RICH front-end electronics is designed to ensure 100% efficiency at 1/3 of the average photo-electron signal level, 1 to 4 gain spread compensation, time resolution of the order of 1 ns to distinguish direct from reflected photon hits, and a trigger rate up to 20 kHz and 8 μs trigger latency.

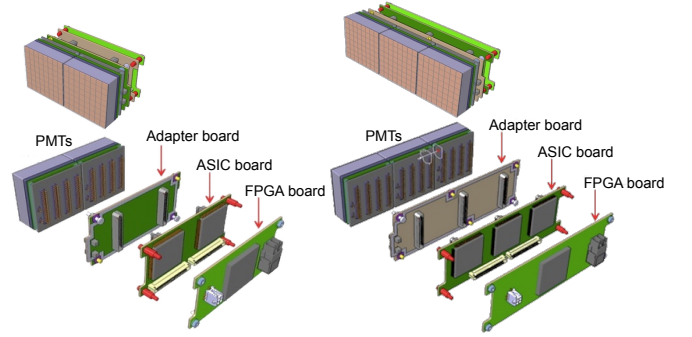


Figure 11: The CLAS12 RICH readout unit design (see text for details).

The front-end electronics is organized in compact units (tiles) mechanically designed to fit the MAPMT dimensions, each serving two or three MAPMTs, thus allowing the tessellation of large surfaces with minimum dead space and material budget, see Fig. 11. Each readout unit comprises three boards with complementary functions.

A feed-through *adapter board* provides the electrical connectivity of the sensors with the external readout system while preserving the adequate light and gas tightness of the inner detector volume when mounted on the RICH carbon fiber supporting panel. It also distributes the sensor bias voltage (with -1000 Volts as nominal value). The *signal processing board* is based on the MAROC3 chip [18], a 64-channel microcircuit dedicated to MAPMT pulse processing. Each channel comprises a low impedance adjustable gain preamplifier followed by two highly configurable shaping sections with independent processing. The first section embeds a slow shaper and a sample and hold structure to allow linear charge measurements up to 5 pC. Requiring short trigger delays and multiplexed access, this feature is used as a RICH calibration tool. The second section features a fast shaper and an adjustable threshold discriminator to produce, for each input signal, a start and stop logic pulse. These are stored in a 8 μs deep circular memory allowing a parallel, almost dead-time free, readout. The fast shaper works in an almost saturated regime to maximize the discrimi-

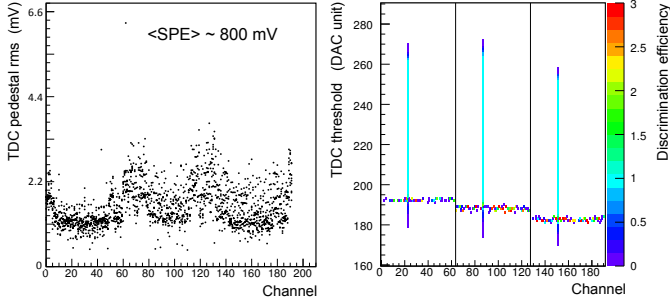


Figure 12: (Left) Pedestal RMS, as measured on a test point, of the 192 channels of the $3\times$ MAROC boards during the production quality assurance. The measured RMS values are below 4 mV while the single photo-electron signal is expected around 800 mV. (Right) Logic discrimination efficiency as a function of the MAROC channel, for a range of programmed thresholds. A test pulse corresponding to 60 fC, i.e. about 1/7 of the expected typical single photo-electron discharge, is generated by the programmable on-board pulse generator and injected in channel 23 of each chip. Close to the pedestal value, spurious fluctuations are discriminated in all channels (efficiency greater than 1). At threshold values below the pedestal, the system digitized the undershoot of the bipolar shaped signal.

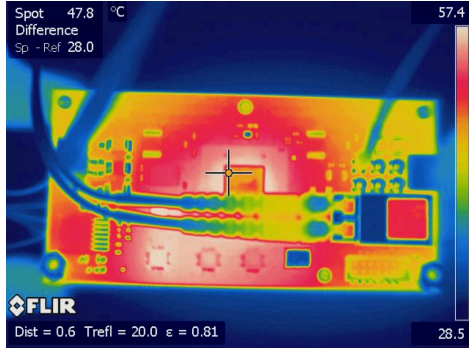


Figure 13: The CLAS12 RICH readout unit design (see text for details).

nation efficiency. The MAROC chip is configured and read out by a *FPGA board* optically linked to the data acquisition back-end (DAQ) using the JLab Sub-System Processor (SSP), which resides in a VXS/VME crate. The current firmware version includes a 1 ns precision timestamping of the logic pulses.

A constant-threshold binary readout requires a good stability of the baseline (pedestal) and definition of the working point (gain and threshold). Their programmed levels are here expressed as Digital-to-Analog Converter (DAC) units. During the board production, quality assurance tests confirmed the excellent sensitivity of the logical readout, able to discriminate signals down to a few percent of a single photon-electron discharge, see Fig. 12.

2.5.1. Characterization

Each readout unit was characterized in laboratory tests using a pico-second precision pulsed PicoQuant laser of 405 nm wavelength. A light diffuser was used in order to uniformly illuminate the whole sensitive area and integrate all the local variations of the sensor response. The laser pulse intensity was tuned and optical neutral density filters added in order to

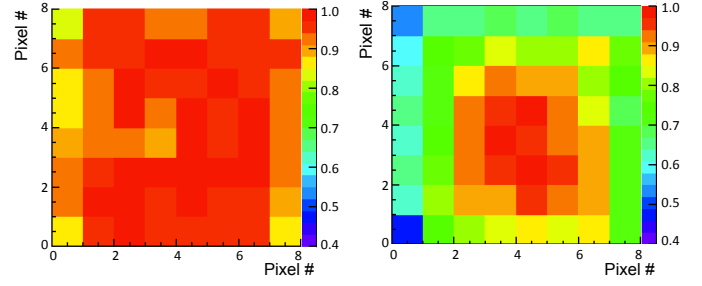


Figure 14: (Left) Example of MAPMT efficiency map normalized to the maximum pixel efficiency. Data show an almost flat behavior at values close to 1 except for the edge pixels. (Right) Example of MAPMT gain map normalized to the maximum pixel gain. The visible 1:2 variation is expected for this type of sensors and can be compensated by the electronics.

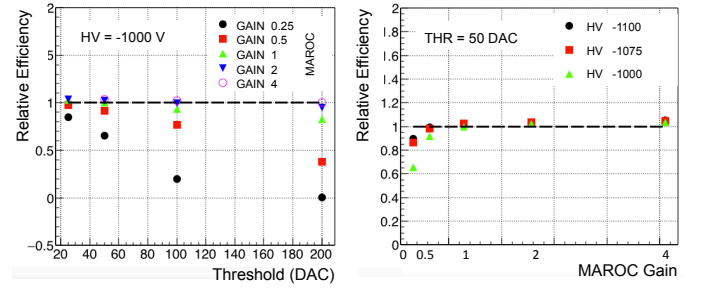


Figure 15: Relative SPE detection efficiency as a function of the working parameters: bias voltage, MAROC preamplification gain and discriminator threshold. The plots show the dependence on two parameters while keeping fixed the third: bias voltage (left) or threshold (right). Data are normalized to the reference point at HV=-1000 V, gain=1 and threshold=+50 DAC. Values greater than 1 are likely due to the cross-talk contribution.

deliver on average 3 photon hits per MAPMT. The recorded single-photon spectra allowed to map the relative gain and efficiency of the 64 pixels of each MAPMT [19], see Fig. 14. All the MAPMTs were fully tested and characterization parameters were extracted by fitting a detailed model of the SPE spectrum, developed at JLab [20]. Data showed that the H12700 has, on average, a 10% better efficiency than the H8500, likely due to the improved photocathode performance. The recorded information can be useful for the likelihood definition of each particle hypothesis in the RICH reconstruction. In addition, the SPE spectra allow to study the efficiency dependence on the working parameters, i.e. MAPMT bias voltage, MAROC preamplification gain and threshold. Data indicated the efficiency reaches a plateau over a wide range of working parameter values, see Fig. 21. The plateau would correspond to the region where all the MAPMT discharges are digitized and the efficiency ultimately depends on the quality of the photocathode. The plateau is a consequence of the saturated mode employed in the MAROC binary readout and allows a flexible definition of the working point, a crucial feature when dealing with a large number of channels in the challenging single-photon regime.

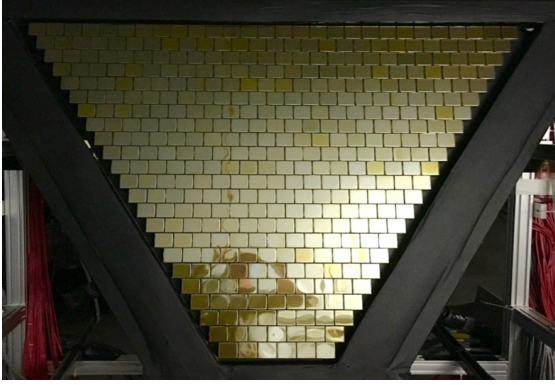


Figure 16: The plane of MAPMTs fully assembled.



Figure 17: The Front End electronics fully assembled and cabled.

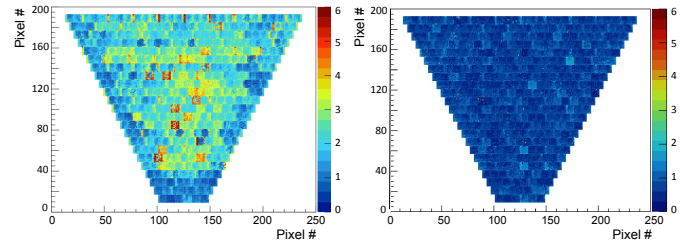


Figure 18: (Left) Pedestal rms values before (left) and after (right) the realization of a grounding grid connecting all the electronic units to the RICH chassis to provide a reference for the floating power lines.

2.6. Services

3. Assembly and preliminary tests

The RICH vessel was mounted on a large Aluminum frame allowing rotations from the vertical to the horizontal position, as required by the various assembling phases. Each inner element was installed on the mechanical structure after the completion of the characterization tests. This assembly phase included also a detailed survey of the position and alignment of each inner element, in particular the mirrors, with respect to the mechanical structure of the detector. The lateral mirrors were the first elements installed followed by the spherical mirror.

The RICH readout system, composed by 138 tiles with 391 MAPMTs for a total of 25024 independent channels, was assembled on a dedicated carbon fiber panel. An independent Aluminum support was employed to get easy access and allow rotations during the functionality tests. The MAPMTs plane is shown in Fig. 16, while the fully assembled Front End electronics is shown in Fig. 17. The complete readout system was eventually moved into the the RICH and the closing panels temporarily mounted on the detector to test of the light and gas tightness of the system, prior of aerogel installation.

The aerogel was the last element installed, being the most sensitive to the external conditions. Each tile were inspected and mounted in a pre-selected location of the supporting element, being the latter a carbon fiber panel (6 cm layer) or a front mirror with the Al frame (2 cm layer). The location was defined depending on the aerogel tile shape and optical quality to maximize the overall performance. During assembling, the aerogel panels were maintained in a low humidity atmosphere (around 20 % relative humidity) to prevent moisture absorption. When ready, they were all mounted at once onto the RICH to allow an instantaneous start of the nitrogen conditioning of the inner RICH volume and minimize the exposure to the external weather conditions.

Several tests have been performed with cosmic rays at various stages of the detector assembling. The photodetectors and the readout electronics were extensively tested using cosmic rays detected by a tracking system installed on a dedicated trigger station inside a large dark box. In the absence of a precise

measure of the cosmic particle momentum it was not possible to perform a study of the Cherenkov angle resolution. Nevertheless, cosmic runs allowed to validate the translation tables relating electronic channels with pixel positions, develop the ring reconstruction software, verify the stability of the system, and test the performance of the services (power supplies, cooling, readout, slow-control, interlock).

Once the detector was sealed and before the transportation to the experimental hall, its functioning parameters were tested for several weeks in the assembly room. The tests included the two gas systems serving the RICH: the nitrogen system that must keep the internal humidity at few percent level to preserve the optical performance of the aerogel and the air cooling system of the readout electronics.

4. Commissioning With Beam

The RICH detector was installed in the CLAS12 experiment at the beginning of January 2018. The electronics pedestal values were regularly monitored during the following engineering run and CLAS12 data-taking, as their stability is a crucial feature for the constant threshold readout.

With the full detector assembled, the measured pedestal RMS was initially at the level of few DAC units. In order to properly refer to the same ground the whole composite readout system, powered by 156 floating 5V low-voltage lines, a grounding grid was realized connecting by a copper wire all the boards with the detector chassis. With the grid, the typical pedestal RMS was

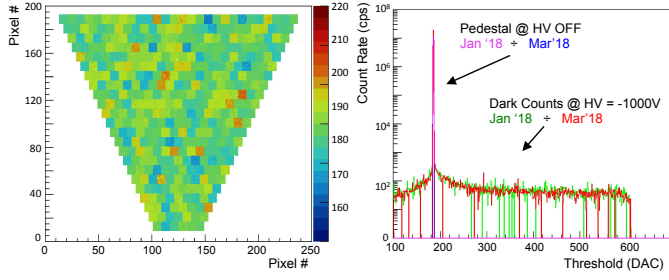


Figure 19: (Left) Pedestal map of the whole MAPMT plane showing the values within the same MAPMT are quite uniform. (Right) Count rate of one MAPMT pixel as a function of the discrimination threshold as measured at the beginning and at the end of the first CLAS12 physics run. A pixel with a dark count rate above the average is chosen for better visibility. The discriminated signals have been recorded within a programmed time window at each of the thresholds selected for the scan. The peak corresponds to the pedestal (when the threshold equals the baseline), visible also at HV OFF. The tails to the dark count signals (bipolar after the shaping section) at HV ON. The shoulders around the pedestal are due to cross-talk signals. The almost flat behaviour up to 600 DAC is due to the large amplification (and almost saturated signals). The pixel behaviour is stable along the time. Color scales and threshold are in DAC units.

reduced to values comparable with the ones measured in the quality assurance tests and at the limit of the readout sensitivity, i.e. at the level of 1 DAC and thus negligible, see Fig. 18.

The pedestal level is different for each MAROC, but is relatively uniform within one chip, a feature conforming to the common discrimination threshold, see the left plot in Fig. 19. With HV ON, the typical measured dark count rate is around 10 Hz/pixel, in agreement with the Hamamatsu specifications. In the right plot of Fig. 19, the measured dark rate of one pixel of a H12700 MAPMT is plotted as a function of the discriminating threshold with MAPMT HV OFF (0 V) and HV ON (-1000 V) at the beginning and at the end of the first physics run. The plot shows a large region of uniform response above a very narrow pedestal (as expected from the laboratory characterization) that stays unchanged over time.

A typical feature of any constant threshold readout is the time-walk, i.e. the dependence of the discrimination time on the signal amplitude. The time-over-threshold (ToT) derived from the recorded start and stop signal times provides a non-linear estimate of the charge collected at the MAPMT anode. This can be used to correct for the time-walk effect. In order to have an easier handling of the time-walk and ToT behavior over the 25000 channels of the RICH detector, an equalization of the SPE shaped pulses is desirable, in particular because the MAROC programmable threshold is common to all its 64 readout channels. The RICH channel-by-channel SPE signal equalization was performed during the CLAS12 engineering run with real data. Data-acquisition tests were made at various thresholds for different MAROC gain configurations. Fig. 20 shows the ToT distribution for three typical values of the threshold: on the left for all channels without amplification (nominal MAROC gain of 1), on the right after equalization (tuning the average MAPMT+MAROC gain to 2.7×10^6 in all the channels). After equalization, the ToT distribution of saturated SPE signals is narrower than before. With typical ToT values larger

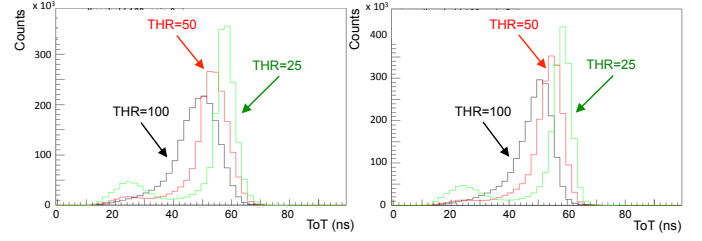


Figure 20: ToT distributions of the RICH channels at three typical values of threshold (25, 50 and 100 DAC) without (left) and with (right) gain equalization. The saturated SPE signals generally yield ToT duration greater than 40 ns. When lowering the threshold also weaker cross-talk signals are recorded with ToT duration around 25 ns.

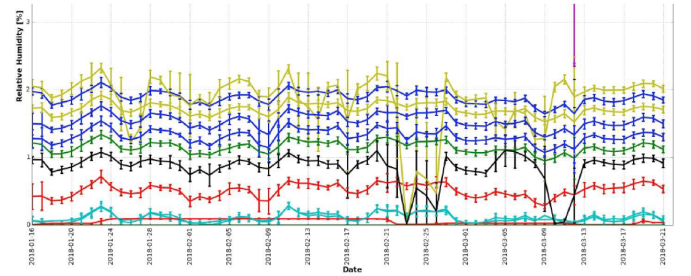


Figure 21: Monitor of the humidity level in the inner RICH volume over the three months of the first CLAS12 data-taking period. The lines (colors) correspond to different sensors positioned in various locations inside the RICH.

than 40 ns, it also is clearly separated from the cross-talk signals whose ToT values distribute around 25 ns.

5. RICH Slow Control

Description and performance

6. RICH Event Reconstruction

The RICH reconstruction is organized into 4 steps.

In the first step, the spatial and time information of each hit is reconstructed taking into account possible misalignments and calibration corrections. If more than 3 hits are found around a local maximum, they are grouped into a RICH cluster. A cluster is typically created by a charged particle producing Cherenkov light into the MaPMT window or ionization into the sensor dynode structure. The time of the cluster is taken to be equal to the time of the local maximum, while its spatial coordinates are calculated as a weighted average over all the hits with their ToT value as the weight. If a sole hit is found close to a local maximum, with an amplitude lower than 80% of that maximum, the hit is flagged as possible cross-talk. The hit should be within a 3x3 MaPMT pixel matrix (nonet) centered on the maximum, or on a MAROC3 input adjacent to the maximum, to be flagged as optical or electrical cross-talk, respectively. This selection rejects about YY% of the cross-talks and further reduction would be only possible with a time versus amplitude analysis, see Fig. 24. The cross-talk selection also removes a

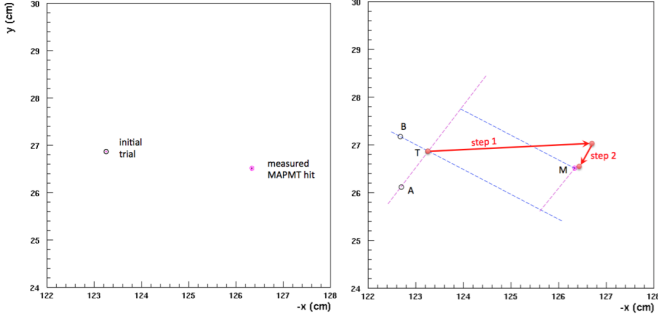


Figure 22: Example of the ray-tracing iterative photon path reconstruction. At each step, the emission polar and azimuthal angles of the trial photon T are varied by the expected Cherenkov angle resolution to extrapolate the detection points A and B. The distance vector $\vec{T}\vec{M}$ between the measured hit M and the trial T is projected onto the displacement vectors $\vec{T}\vec{A}$, corresponding to an angular shift of $\delta\theta$, to estimate the scale factor f of the wanted angular step $\Delta\theta = f\delta\theta$ with $f = (\vec{T}\vec{M} \cdot \vec{T}\vec{A})/|\vec{T}\vec{A}|^2$. The same is done for the azimuthal angle ϕ .

small 3% fraction of true single photo-electron signals. Those correspond to SPE signals that undergo an incomplete dynode multiplication, while being by chance close in space to an independent standard SPE signal. Cross-talk hits are not considered further in the RICH reconstruction.

In the second step, RICH clusters are associated to the CLAS12 tracks if a match in space is found, i.e. the extrapolated impact point of the track into the MaPMT plane is closer than 10 cm to the cluster center. Matched clusters allow a precise study of the MaPMT detector position and orientation relative to the CLAS12 tracking system, see Fig. ??.

The third step is the core of the RICH reconstruction. For each hit in the MaPMT plane, an estimate of the corresponding Cherenkov angle is derived by ray-tracing the photon path inside the RICH volume taking into account possible reflections. This is done in turn for each particle traced through the RICH, with the photon emission point assumed to be the middle point of the particle path inside the aerogel radiator.

In the fourth step a particle identification algorithm is applied using an event-based likelihood of the reconstructed Cherenkov angles.

The photon path inside the RICH is reconstructed in two complementary ways. The first is an analytic formula that takes into account the refraction at the aerogel face and is only valid for directly detected photons. It provides an exact solution that derives the correct aerogel refractive index in conjunction with the reconstructed Cherenkov angle. The second is a ray tracing algorithm that takes into account also the mirror reflections. The relevant RICH components (aerogel, mirrors, MaPMT plane) are converted into ray-tracing planes or spheres where the photon undergoes refraction, reflection or detection.

Each ray-tracing element can be independently aligned. The alignment procedure uses as benchmark the Cherenkov signal generated by particles identified as electrons by CLAS12 sub-detectors other than RICH. For these particles, the expected Cherenkov angle is given by the known particle momentum and mass. The position and orientation of the MaPMT plane is de-

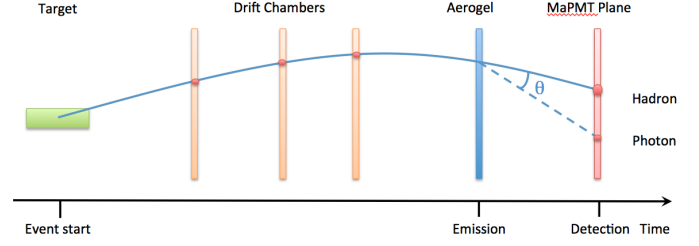


Figure 23: The photon detection time as measured by the RICH can be compared to the more precise time extrapolated by the CLAS12 spectrometer. The latter is defined as the event start time plus the flight-times of the hadron from the interaction point to the radiator center, and of the ray-traced photon within the RICH volume. Any systematic difference emerging as the average over several events provides a mean of calibration for the RICH time. After calibration, a time coincidence within the event can be used to validate the single photon reconstructed path and emission point.

finned by minimizing the average matching distance of the RICH clusters from the extrapolated DC tracks. Each other RICH ray-tracing element can be aligned with respect to the MaPMT plane by selecting the sub-sample of photons passing through that component. The alignment is made by minimizing the average distance between the ray-traced detection point (rdp) and the corresponding measured MaPMT hit over the selected sub-sample of photons.

For each hadron track, the ray-tracing algorithm progresses as described in the following. A limited ensemble of hypothetical photons (about 50) is traced assuming an initial particle hypothesis (electron for a particle identified as electron in CLAS12, pion otherwise). These photons, called trials, are assumed to originate at the emission point at a Cherenkov angle θ_0 , corresponding to the given particle hypothesis, and at an azimuthal angle ϕ_0 , uniformly distributed around the charged particle trajectory. Their ray-traced detection points provide a reference path for the reconstruction. For each MaPMT measured hit, the closest rdp at a distance smaller than 10 cm is taken to be the starting point of the ray-tracing procedure for that hit. An estimate of the angular distance between the trial and measured photon $\Delta\theta = f\delta\theta$ is estimated by ray-tracing a test photon with the angle $\theta = \theta_0 + \delta\theta$ varied by the SPE angular resolution $\delta\theta$. On the MaPMT plane, an estimate of the factor f can be obtained as the scalar product of the vector connecting the trial to the measured hit with the vector connecting the trial to the test rdp, see Fig. 22. A negative f signals a wrong choice of the test direction. The same is done for the azimuthal ϕ angle. A new trial photon is traced with the angles changed by such calculated angular shifts ($\theta_0 + \Delta\theta$, $\phi_0 + \Delta\phi$) and the procedure repeated. At each step the trial rdp gets closer to the measured hit, but an exact solution can not be found as the procedure uses a linear approximation relating the distances in the MaPMT plane with the angular shifts in the 3D space. The iterative procedure stops when the distance of the trial rdp to the measured hit is smaller than half of the MaPMT pixel size (RICH detector spatial resolution). The converge is fast, typically within 3 steps.

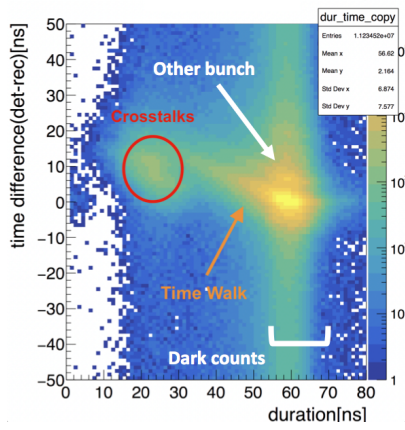


Figure 24: Typical online plots showing the cumulative distribution of the difference ΔT between RICH measured and CLAS12 extrapolated times as a function of the hit duration. Several features are highlighted. Single photoelectron MaPMT discharges concentrate at 60 ns duration. The single channel time-offsets result in a broad peak of Cherenkov signals around ΔT equal zero, whereas the off-time band corresponds to random dark counts or wrong beam bunches. The time-walk of small SPE signals, generated by the constant threshold readout, is visible as a drifting tail at smaller duration times. An independent excess around 20 ns duration times signals a residual contamination of cross-talk signals.

7. RICH Time Calibration

The reconstructed photon path and angle are validated by $\pm 3\sigma$ ns time coincidence between the RICH recorded time and the CLAS12 expected time, where σ is the estimated single photon-electron time resolution, see Fig. 23. The expected time is defined as the event start time of the beam particle primary interaction with the target plus the flight time of the produced hadron to the aerogel radiator and of the ray-traced photon to the sensor. The CLAS12 expected time much smaller time uncertainty than RICH, being defined by a precise time-of-flight system with better than 0.1 ns time precision corrected with the beam radio-frequency clock [26]. The hadron trajectory is calculated taking into account the magnetic field inhomogeneities and fringes [27].

The difference ΔT of the RICH measured time from the more precise CLAS12 extrapolated time provides a practical way to calibrate the RICH time, estimate the RICH time resolution and identify spurious signals, see Fig. 24.

The cumulative ΔT distribution over several events is used to measure and monitor the time-offset of each of the 25 thousands RICH readout channels, see Fig. 26. Individual time-offsets are due to the specific front-end chip performance, readout circuit routing and data-acquisition fiber-optic length, in conjunction with the configuration details of the CLAS12 trigger distribution system which may vary during the data-taking.

The dependence of ΔT over the signal duration time is fitted to extract the time-walk dependence. The fit assumes two linear dependences with different slopes, one in the saturated region around 60 ns duration times, one for unsaturated signals at smaller duration times. The exact point separating the two regimes is also defined by the fit. The time-walk is a feature

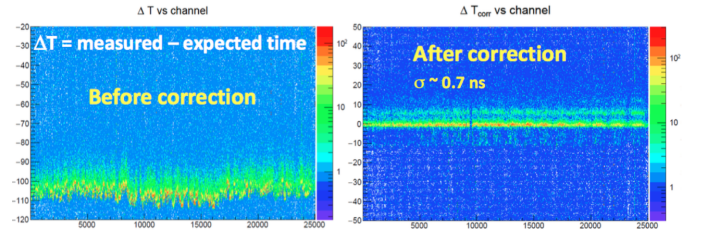


Figure 25: Distribution of the time difference ΔT between measured RICH and extrapolated CLAS12 times as a function of the RICH readout channel. On the left before and on the right after the RICH time-offset calibration.

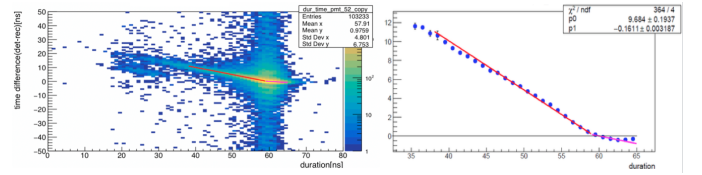


Figure 26: Example of time-walk correction. On the left the distribution of photon signals after the time-offset calibration. The fit function is highlighted in red. On the right the detail of the fit, performed over the average time values calculated in bins of time duration.

ture of the constant threshold readout and ultimately depends on the intrinsic MAROC3 shaping signal configuration. As a consequence, it is not expected to vary over the MaPMT channels readout by the same chip, and to not depend on the data-acquisition and trigger distribution configuration details. This feature has been validated by data. Despite the time-offsets change with the run conditions, the time-walk appears to be relatively stable during the data-taking. Being almost independent by the single channel behaviour, the time-walk fit is done at MaPMT level, integrating the signals of all the pixels.

8. Performance During the Physics Run

After calibration, the typical time resolution is of the order of 0.7 ns and well within the RICH specification to be less than 1 ns, see Fig. 27. Such a time resolution is instrumental to suppress the spurious signals highlighted in Fig. 24, and to identify direct and reflected photon paths. A photon that is reflected back by the spherical mirror, and undergoes a second reflection towards the photon detector, travel a distance almost three times longer than a direct photon, resulting in a time difference of the order of 6 ns.

Examples of reconstructed RICH events are shown in Fig. 28. A remarkable feature is the low level of spurious hits from accidentals, in-time background (i.e. Rayleigh scattering) and dark counts. This feature is crucial for the most challenging cases: particles with high momenta close to the 8 GeV limit that require the best resolution in Cherenkov angle, and particles pointing towards the spherical mirror whose number of detected photons is limited by the double reflection and a second passage through the radiator.

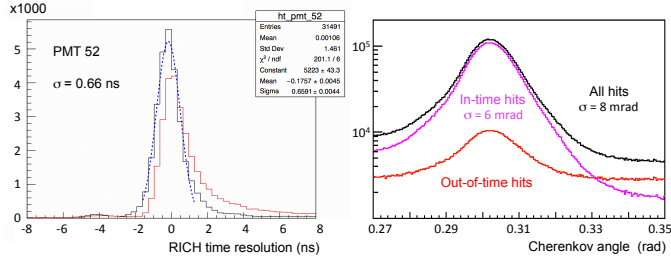


Figure 27: (Left) Typical time resolution before (red) and after (blue) time-walk correction for all the pixels in MAPMT 52. (Right) Cherenkov angle reconstruction without (black) and with (magenta) a time coincidence request between RICH detected and CLAS tracking times (the difference is in red).

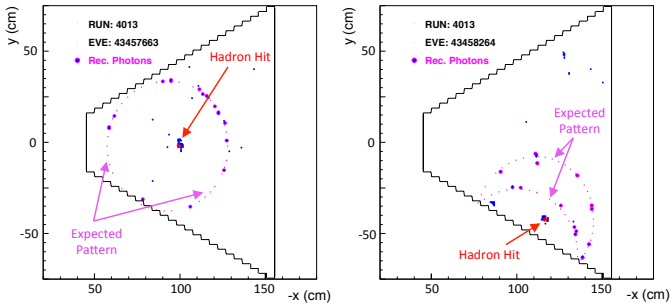


Figure 28: Examples of RICH reconstructed events: direct (left) and partially reflected (right). Big dots indicate the reconstructed photon hits. The arrows indicate the hadron impact point (red star) and the expected photon pattern (small magenta points).

Each aerogel tile presents specific features because the challenging production process, tuned to achieve the highest transparency over a large volume, is not fully industrialized. The most important quality parameters are the density, related to the average refractive index, homogeneity, related to the refractive index variations within the volume, and tile bending, originated by the inner material tension and related to the surface planarity. The effect of these features to the RICH reconstruction can be studied in details using the control sample of electrons identified by CLAS12. In the 2 to 8 GeV/c momentum range relevant for RICH, the Cherenkov cone generated by an electron is saturated to the maximum aperture angle corresponding to the low mass of the particle. Given the large number of tiles and the broad range of particle directions after the CLAS12 bending magnets, such a study requires a large statistics and is still ongoing. A similar approach is used for the alignment study. Also in this case, a large statistics is needed due to the numerous involved components (aerogel layers, mirrors and MaPMT plane) and photon path configurations. Despite the above studies have not been finalized yet, and only partial corrections have been implemented so far, the preliminary SPE Cherenkov angle resolution yields about 6 mrad, see Fig. 27. It is expected to improve towards the goal value of 4.5 mrad once the corrections for the detector misalignment will be implemented and the realistic optical parameters of each aerogel tile will be accounted for. As an example, the effect of a preliminary alignment of the

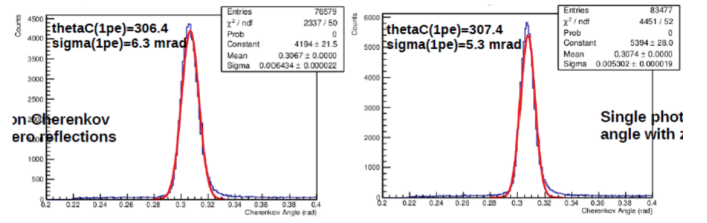


Figure 29: RICH Cherenkov resolution before (left) and after (right) a preliminary RICH alignment. The whole RICH detector is aligned minimizing the matching distance between RICH clusters and extrapolated DC tracks. No possible misalignment of the single RICH component is accounted for. The distribution is for particles passing through one aerogel tile of 2 cm thickness (tile 12 in layer 1) and for direct photons.

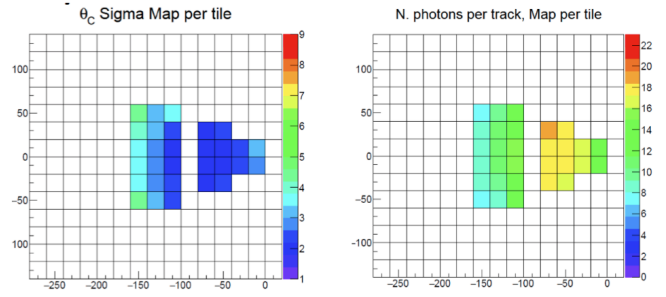


Figure 30: Example of a tile dependent analysis for the aerogel of 2 cm thickness. Average number of reconstructed photons (left). Average Cherenkov angle resolution (right).

whole RICH detector (not taking into account possible single component misalignments) is shown in Fig. 29.

As a general approach, the RICH performance is studied separately for each aerogel tile, see Fig. 30. The RICH global performance estimators are then defined by averaging the results over all the radiator tiles. The preliminary Cherenkov angle resolution is already sufficient for an effective hadron separation in the goal range of momenta, from 3 to 8 GeV/c, as shown by Fig. 31 and Fig. 32.

9. Conclusions

Preliminary data analysis shows that the CLAS12 RICH, for the first time equipped with H8500 and H12700 MAPMTs, is able to match the required time and Cherenkov angle resolution. A compact and scalable readout electronics system has been realized for the detector, able to work in the single-photon regime with high efficiency and stability. It provides a reliable readout system for a variety of cutting-edge sensors, from densely packed H13700 MAPMTs to novel SiPM matrices.

10. Acknowledgments

This material is based upon work supported by INFN, Italy and by the U.S. Department of Energy, Office of Science, Office of Nuclear Physics under contract DE-AC05-06OR23177 and

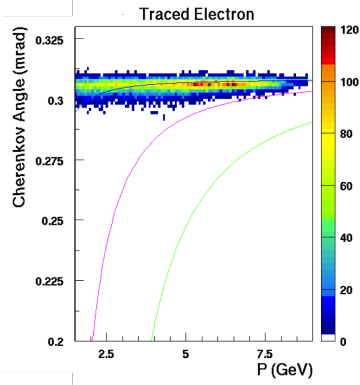


Figure 31: RICH response for electron particles as identified by CLAS12. As expected, the measured Cherenkov angle is saturated over the whole momentum range, from 3 GeV/c up to 8 GeV/c. The distribution is for particles passing through one aerogel tile of 2 cm thickness (tile 12 in layer 1) and direct photons.

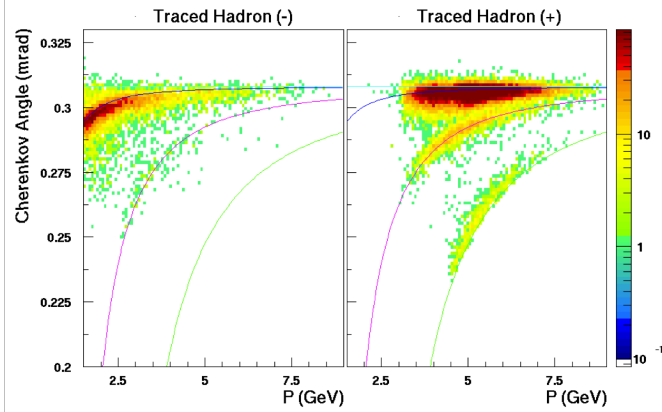


Figure 32: RICH response for non-electron particles as defined by CLAS12. The measured Cherenkov angles distribute around the expected pion, kaon and proton values depending on the momentum. The three hadron population are separated over the whole momentum range, from 3 GeV/c up to 8 GeV/c. The distribution is for particles passing through one aerogel tile of 2 cm thickness (tile 12 in layer 1) and direct photons resulting in a peculiar momentum distribution.

the National Science Foundation, Award #1615067. We thanks the JLab Detector Support Group and Fast Electronic Group, the Hall-B technical and management staff and the INFN technical and administrative service.

[1] CLAS12 Technical Design Report, version 5.1 208 (2008).
[2] J. Dudek *et al.*, *Eur.Phys.J.* **A48** (2012) 187.
[3] H. Avakian *et al.*, *arXiv:1202.1910v2 [hep-ex]* (2012).
[4] M. Contalbrigo *et al.*, *Nucl. Instrum. Meth.* **A 639** (2011) 302.
[5] A. El Alaoui *et al.*, *Physics Procedia* **37** (2012) 773.
[6] S. Anefalos Pereira *et al.*, *Eur. Phys. J. A* **52** (2016) 23.
[7] <http://www.tecnavan.it/en/>
[8] R. De Leo *et al.*, *Nucl. Instrum.Meth.* **A 595** (2008) 19; A. Yu. Barnyakov *et al.*, *Nucl. Instrum. Meth.* **A 453** (2000) 326; R. Pereira *et al.*, *Nucl. Instrum. Meth.* **A 639** (2011) 37; R. Forty *et al.*, *Nucl. Instrum. Meth.* **A 623** (2010) 294.
[9] T. Iijima *et al.*, *Nucl. Instrum. Meth.* **A 598** (2009) 138.
[10] M. Contalbrigo *et al.*, *Nucl. Instrum. Meth.* **A876** (2017) 168.
[11] E. Aschenauer *et al.*, *Nucl. Instrum. Meth.* **A 440** (2000) 338.
[12] <http://www.compositemirrors.com/>

[13] <https://www.evaporatedcoatings.com/>
[14] <http://www.media-lario.com/>
[15] https://www.hamamatsu.com/resources/pdf/etd/H8500_H10966_TPMH1327E.pdf.
[16] R. A. Montgomery *et al.*, *Nucl. Instrum. Meth.* **A 695** (2012) 326.
[17] https://www.hamamatsu.com/resources/pdf/etd/H12700_TPMH1348E.pdf.
[18] S. Blin *et al.*, *IEEE Nucl. Sci. Symp. Conf. Rec.* **2010** (2010) 1690.
[19] M. Contalbrigo *et al.*, *Nucl. Instrum. Meth.* **A 787** (2015) 224.
[20] P. Degtiarenko, *arXiv:1608.07525*.
[21] F. Barbosa *et al.*, *Nucl. Instrum. Meth.* **A 876** (2017) 69.
[22] C.P. Wong *et al.*, *Nucl. Instrum. Meth.* **A 871** (2017) 13.
[23] A. Del Dotto *et al.*, *Nucl. Instrum. Meth.* **A 876** (2017) 237.
[24] https://www.hamamatsu.com/resources/pdf/etd/H13700_TPMH1370E.pdf.
[25] https://www.hamamatsu.com/resources/pdf/ssd/s13361-3050_series_kapd1054e.pdf.
[26] D. Carman *et al.*, *This volume*
[27] M. Mayster *et al.*, *This volume*